# Photoreforming of poly(ethylene-terephthalate) plastic into valuable chemicals and hydrogen over BiVO4/MoOx: Synergistic promotion of oxidation and reduction processes

Xinxin Liang, Ting Gao, Yongqian Cui, Qibing Dong, Ximing Li, Abdelkader Labidi, Eric Lichtfouse, Fei Li, Feng Yu, Chuanyi Wang

Applied Catalysis B: Environment and Energy 357 (2024) 124326

https://doi.org/10.1016/j.apcatb.2024.124326

# Photoreforming of poly(ethylene-terephthalate) plastic into valuable chemicals and hydrogen over $BiVO_4/MoO_x$: Synergistic promotion of oxidation and reduction processes

Xinxin Liang [a], Ting Gao [a], Yongqian Cui [a], Qibing Dong [a], Ximing Li [a], Abdelkader Labidi [a], Eric Lichtfouse [d], Fei Li [a,*], Feng Yu [c], Chuanyi Wang [a,b,**]

[a] School of Environmental Science and Engineering, Shaanxi University of Science and Technology, Xi'an 710021, PR China
[b] Jiangxi Key Lab of Flexible Electronics, Flexible Electronics Innovation Institute, Jiangxi Science and Technology Normal University, Nanchang, Jiangxi 330013, PR China
[c] Key Laboratory for Green Processing of Chemical Engineering of Xinjiang Bingtuan, School of Chemistry and Chemical Engineering, Shihezi University, Shihezi 832003, PR China
[d] State Key Laboratory of Multiphase Flow in Power Engineering, Xi'an Jiaotong University, Xi'an, Shaanxi 710049, PR China

ARTICLE INFO

*Keywords:*
$H_2$ evolution
$MoO_x$ particle
Photoreforming plastic
Polarization effect
Valuable chemical

ABSTRACT

Photoreforming plastic waste into value-added chemicals along with hydrogen evolution is crucial for the circular economy, but its efficiency is limited by mutual constraints between proton reduction and plastic oxidation. Herein, $MoO_x$ particles were decorated onto $BiVO_4$ attempting to promote photo-redox reactions, simultaneously. Experiments and theoretical calculations demonstrate that oxygen vacancy in $MoO_x$ promotes the adsorption of pretreated poly(ethylene-terephthalate), leading to enhanced oxidation of poly(ethylene-terephthalate). Meanwhile, $MoO_x$ boosts the transfer of photoelectrons from $BiVO_4$ to $MoO_x$ by $Mo^{5+/6+}$ ions with variable valence states and lowers the free energy of $H^+ + e^- \rightarrow H^*$ from 0.39 to –0.12 eV, thereby promoting $H_2$ evolution. Consequently, the photoreforming efficiencies of converting poly(ethylene-terephthalate) into formate, acetate and $H_2$ by $BiVO_4/MoO_x$ are 0.29, 0.19 and 1.96 mmol $g^{-1}$ $h^{-1}$, which are respectively 6.2, 6.0 and 5.9 times higher than that by $BiVO_4$. This work presents avenues for designing high-performance catalysts to efficiently photo-reform plastic.

## 1. Introduction

Plastics have become a necessity in modern life and production of industrial products due to their affordability, stability, and processability, while more than 70 % of plastics are wasted in natural environment [1]. The spontaneous degradation of waste plastic typically takes hundreds of years because of the high chemical stability [2], resulting in serious environmental problems [3]. Moreover, the release of plastic waste has become a worldwide pollution emergency, with around 10 million metric tons of plastic entering into the Earth's oceans annually [4]. Traditional methods of plastic disposal are landfilling, incineration and secondary recycling, while these methods are incapable of sustainably and economically recycling the plastic waste. Taking landfill as an example, the plastic waste can be easily handled, but it requires a large amount of land, changes the pH of soil, and affects the sustainable use of land [4,5]. Given this situation, it is tremendously necessary to explore sustainable and economically beneficial strategies for plastic conversion.

Plastic can be converted into fuel or valuable chemicals by reforming, in particular thermoreforming, electroreforming and photoreforming [6]. Photoreforming of plastic waste appears very promising due to the unlimited availability of solar energy [7]. Polyethylene terephthalate (PET) is one of the most commonly used plastic materials, typically employed to produce water bottles and packaging boxes [8]. Therefore, the photoreforming of PET has attracted wide attention. In a typical photoreforming process, the photogenerated electrons and holes in a photocatalyst are transported to the surface, where they actively engage in redox reactions. However, the photoreforming performance is

* Corresponding author.
** Corresponding author at: School of Environmental Science and Engineering, Shaanxi University of Science and Technology, Xi'an 710021, PR China.
*E-mail addresses:* fayeli@sust.edu.cn (F. Li), wangchuanyi@sust.edu.cn (C. Wang).

severely restricted by limited proton supply and slow oxidation process. Therefore, in the photoreforming of PET, it is highly desired to simultaneously enhance the hydrogen evolution reaction (HER) and facilitate the oxidation of plastic substrates.

Due to the insolubility of PET waste, it is generally hydrolyzed into terephthalate (TPA) and ethylene glycol (EG) in alkaline conditions, and only EG participates in the photoreforming process [9]. For example, Reisner et al. converted EG molecule into formate, glycolate and acetate, meanwhile, hydrogen ($H_2$) was generated from water ($H_2O$) [10]. Additionally, EG can be regarded as a sacrificial agent because it is preferentially oxidized compared to the oxidation of $H_2O$. Therefore, the photoreforming reaction of pretreated PET into $H_2$ and chemicals is nearly energy neutral [11]. As a result, the focus of PET photoreforming should be on the usage of narrow bandgap photocatalysts.

Monoclinic $BiVO_4$ is considered to be one of the most promising narrow-bandgap photocatalysts due to its high visible light response and good chemical stability [12]. However, its poor charge carrier transport properties and sluggish surface reactions constantly limit its photocatalytic efficiency [13]. Metal oxide particles are composed of a small number of atoms, which can expose massive active sites, making them highly beneficial for rapid redox reactions [14]. Moreover, when metal oxide particles are loaded onto photocatalysts, they can induce discrete energy bands to trap charge carriers, thereby facilitating the efficient separation of photogenerated electron-hole pairs [15]. Based on this, the use of particle catalysts to modify $BiVO_4$ holds the potential to enhance the activity of PET photoreforming.

The properties of metal oxide particle cocatalysts are dramatically influenced by the number and coordination environment of the active atoms [16]. Therefore, it is crucial to develop an approach that accurately controls the morphology of particles decorating the surface of photocatalysts. Herein, a simple hydrothermal strategy is developed to anchor molybdenum-oxygen ($MoO_x$) particles on the surface of $BiVO_4$ ($BiVO_4/MoO_x$). As shown in Scheme 1, benefiting from the low conduction band position and the variable valence $Mo^{5+/6+}$ ions, $MoO_x$ can be regarded as an electron relay, enhancing the transfer of photogenerated electrons from $BiVO_4$ to $MoO_x$. This process reduces the free energy of $H^+ + e^- \rightarrow H^*$ from 0.39 to –0.12 eV, thus facilitating the evolution of $H_2$. Besides, the oxygen vacancy ($O_v$) in $MoO_x$ promotes the adsorption of pretreated PET, leading to enhanced oxidation of PET. As a result, cooperative photo-redox reactions in the process of PET photoreforming are achieved. The optimum activity of $BiVO_4/MoO_x$ for PET photoreforming into formate, acetate and $H_2$ reach 0.29, 0.19 and 1.96 mmol $g^{-1}$ $h^{-1}$, which are 6.2, 6.0 and 5.9 times higher than that of $BiVO_4$, respectively. In short, the designed catalyst $BiVO_4/MoO_x$ can break through the mutual restraints of redox reactions in the photoreforming process of PET, thus leading to excellent performance over most previously reported non-toxic photocatalysts.

## 2. Experimental section

### 2.1. Synthesis of catalysts

#### 2.1.1. Synthesis of pure $BiVO_4$

The synthesis of pure $BiVO_4$was performed by adopting a protocol previously reported [17]. In a specific experiment, 1 mmol of $Bi(NO_3)_3$ and 0.5 mmol of citric acid were added into a 100 mL Teflon-lined autoclave containing 70 mL of deionized (DI) water. The mixture was then heated at 180 °C for 10 h. The white powder obtained was centrifuged at 10,000 revolutions per minute and then cleaned with DI water. Afterwards, the powder was dried at 60 °C under vacuum. Subsequently, light yellow $Bi_2O_3$ powder was obtained by calcination in air at 500 °C for 3 h. Finally, 2 mmol $Bi_2O_3$ powder and 2 mmol $V_2O_5$ powder were added to a $HNO_3$ solution (100 mL, 0.5 M) and stirred for 4 days at 25 ℃. The obtained vivid yellow powder was then cleaned with DI water and dried at 60 °C for 1 day.

#### 2.1.2. Preparation of the $BiVO_4/MoO_x$

$BiVO_4/MoO_x$ photocatalysts were prepared using a hydrothermal method. In a typical procedure, 1 g of $BiVO_4$ and 0.1 g of $(NH_4)_6Mo_7O_{24}{\cdot}4\ H_2O$ were mixed and transferred into a 100 mL Teflon-lined autoclave containing 70 mL of DI water, heated at 180 °C for 10 h. The resulting solid product was obtained by centrifugation at 10000 revolutions per minute, washed with DI water for five times, and dried overnight. Different amounts of $(NH_4)_6Mo_7O_{24}{\cdot}4\ H_2O$ (0.05 g, 0.10 g, 0.15 g) were added, and designated as $BiVO_4$/0.05 $MoO_x$, $BiVO_4$/0.10 $MoO_x$, and $BiVO_4$/0.15 $MoO_x$.

### 2.2. Photocatalysts characterization

XRD patterns of all samples were confirmed using a Smart Lab 9 kW-diffractometer with Cu Kα radiation in the range from 10 to 70° (λ = 1.5406 Å 40 kV and 100 mA). The Raman spectroscopy measurements were conducted using a Raman-microscope (Thermo-Fisher Scientific DXRxi incorporated with a 532 nm laser). The surface morphologies, elemental distribution, and lattice fringes of all samples were analyzed by scanning electron microscope (SEM-ZEISS Sigma 300) and high-resolution transmission electron microscope (HRTEM-JEOL JEM-F200). Micromeritics ASAP 2460 analyzer was used to assess the

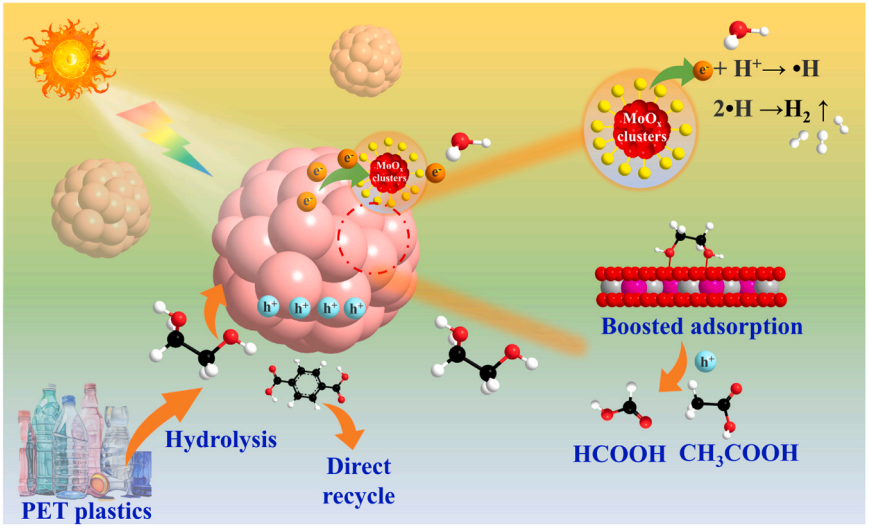


**Scheme 1.** Schematic description of PET plastic photoreforming at $BiVO_4/MoO_x$.

concrete surface areas and pore size distributions for all the prepared materials. X-ray photoelectron spectroscopy (XPS) analyses were conducted on a Shimadzu/Kratos AXIS SUPRA system (hν = 1486.6 eV) at 12 kV and the binding energies of each element were corrected with C 1 s as the standard peak (284.6 eV). The element contents of materials were determined by an inductively coupled plasma optical emission spectrometry (ICP-OES). Ultraviolet photoelectron spectroscopy (UPS-Thermo ESCALAB 250XI) studies were conducted applying He I light source (21.22 eV). UV–visible diffuse reflectance spectra were recorded on an Agilent Cary 5000 spectrophotometer. The surface photovoltage spectroscopy (SPV) and field-induced surface photovoltage spectroscopy (FISPS) measurements were performed on a surface photovoltage spectrometer (CEL-SPS1000). The decay time spectra were recorded on a fluorescence spectrometer (FS5, Edinburgh Instruments Ltd.). The temperature-programmed desorption (TPD) of $H_2O$ measurements were performed on a chemisorption apparatus (XIANQUAN TP-5080). The fluorescence lifetimes for pure $BiVO_4$ and $BiVO_4$/0.10 $MoO_x$ were measured with excitation and emission at 380 nm and 600 nm, respectively. $^1H$ NMR spectra were measured using a 500 MHz Bruker spectrometer. Electron spin resonance (ESR) analyses were conducted using a Bruker E-500. To capture the hydrogen radicals (•H) and hydroxyl radicals (•OH) during irradiation, a dispersion of catalyst containing 100 mM 5,5-dimethyl-1-pyrroline N-oxide (DMPO) was used, with a volume of 1.0 mL. The $\bullet O_2^-$ was tested under the same condition as •H and •OH, with the only difference being that $CH_3OH$ was used as the solvent. In situ FTIR analysis was conducted by Nicolet iS50 FT-IR spectrometer (Thermo-Fisher Scientific) with a mercury-cadmium telluride (MCT) detector. Photoelectrochemical measurements were executed in a three electrodes system with 0.5 M $Na_2SO_4$ as the electrolyte solution. A platinum net electrode, saturated calomel electrode and sample films were used as the counter electrode, reference electrode and working electrode (WE), respectively. The production processes of WE are described as follows: 5.0 mg of the photocatalyst was mixed in solvent including 100 μL of DI water, and 100 μL of ethanol and agitated under ultrasound for 3 minutes. Then, 100 μL of the suspension was applied to ITO with an area of 1 $cm^2$. The experiment was conducted with a 300 W xenon lamp, and the distance between WE and light source was 15 cm.

### 2.3. Plastic upcycling processes

#### 2.3.1. Pretreatment of plastic

A cutting machine was used to cut 25 g of commercial PET granules into smaller particles. 1 g of as-obtained PET powder was mixed with 50 mL of 1 M KOH aqueous solution and stirred in the dark at 50 ℃ for 48 h. The supernatant was collected by centrifugation at 10000 revolutions per minute and used as raw material for photoreforming.

#### 2.3.2. Photoreforming of PET

The photoreforming experiments of PET were conducted in a self-made photoreactor at temperature of 15 °C, under Xe lamp irradiation of 300 W. 50 mg of photocatalyst was added into 50 mL of supernatant collected from PET pretreatment. The mixture was agitated under ultrasound for 3 mins, and then Ar gas was used to exhaust the reactor and create an inert atmosphere for 30 mins.

#### 2.3.3. Products analysis

The evolving $H_2$ was assessed through a meteorological analyzer (FULI GC9720 Plus) with Ar as the carrier gas. Isotopic labeling tests were conducted with substitute $D_2O$/NaOD for $H_2O$/KOH, and the gaseous products in the self-made photoreactor (100 μL) were quantified through a gas chromatograph-mass spectrometer (Shimadzu GCMS-QP2020NX). The composition and concentration of PET hydrolysate were analyzed using $^1H$ NMR spectra both before and after reaction. In a typical experiment, 0.3 mL of a liquid sample was mixed with 0.3 mL of $D_2O$ and 0.1 mL 1 mmol of maleic acid standard. High-performance liquid chromatography (HPLC, Shimadzu-LC-2030 C) carrying with an AMINEX®HPX-87 H column (300 mm × 7.8 mm) and UV detector were utilized to separate and analyze the liquid products from photoreforming hydrolysate of PET. The elution phase and mobile phase were consisted of methanol/$H_2O$ (1:1) and 10 mM $H_2SO_4$ solution, respectively and the flow rate of mobile phase was 10 μL/s.

### 2.4. Computational details

All DFT calculations were performed using a Vienna Ab initio Simulation Package (VASP) with a project-augmented wave (PAW) method [18,19]. The exchange-functional was conducted by the generalized gradient approximation (GGA) of Perdew-Burke-Emzerhof (PBE) functional [20], and the dispersion interactions were presented by Grimme's DFT-D3 methodology [21]. H 1 s, O 2s2p, V 3d4s, Mo 4d5s and Bi 6s6p electrons were treated as valence electrons, as well as the spin-polarized effects of the electrons considered during the calculations. The valence electronic states were expanded in plane-wave basis sets with an energy cutoff at 450 eV.

The $BiVO_4$ was modelled as a redefined two-$Bi_4V_4O_{16}$-layer $BiVO_4$(010) slab (7.3 × 14.8 × 14.5 Å) based on the TEM results (Fig. 2b), and the $MoO_3$ was modelled as a redefined p(1 × 2) $MoO_3$(010) slab (7.5 × 15.1 × 11 Å). The heterojunction (7.3 × 14.8 × 32.2 Å) was constructed by adding one $MoO_3$ layer on each side of $BiVO_4$, with a small lattice mismatch of ~2 %. The k-point mesh was employed as 2 × 1 × 1, and the vacuum thickness between slabs was ~15 Å. All the atoms except the bottom V-Bi-O in the $BiVO_4$ slab and the bottom Mo-O-V-Bi-O in the heterojunction were allowed to relaxed until the atomic force threshold of 0.05 eV/Å. The DOS of independent $BiVO_4$ and$MoO_3$ were leveled relative to the deep energy level of gas $N_2$.

## 3. Results and discussion

### 3.1. Photocatalysts characterization

The XRD patterns of $BiVO_4$ with different Mo contents at 15.13°,19.0°, 28.9°, 30.7°, 35.3°, 42.5°, 47.3° and 53.3° correspond to the (020), (011), (121), (040) (002), (051), (042) and (222) planes of monoclinic $BiVO_4$ (JCPDS No. 14–0688) (Fig. 1a), while there are no characteristic peaks for $MoO_x$ due to its low content and high dispersion [22]. Besides, the characteristic peaks of $BiVO_4$/$MoO_x$ exhibit a slight shift towards higher angles as the $MoO_x$ loading increases in comparison with pure $BiVO_4$. Consequently, the presence of $MoO_x$ particles induce the crystal lattice distortion of $BiVO_4$. In addition, FT-IR spectral analysis (Fig. S1) was conducted to confirm the structure of $BiVO_4$ and $BiVO_4$/0.10 $MoO_x$ photocatalysts [23]. All the IR peaks are attributed to the characteristic peaks of $BiVO_4$, which is in accordance with the XRD results.

As shown in Fig. 1b, the characteristic peaks at around 824, 367, 330 and 211 $cm^{-1}$ appear, which are assigned to monoclinic $BiVO_4$ in all photocatalysts [24]. Additionally, the peak at around 824 $cm^{-1}$ is the most intense, which corresponds to the symmetric V–O stretching, the other peaks are in accordance with the symmetric V–O bending (367 $cm^{-1}$), antisymmetric V–O bending (330 $cm^{-1}$), and external mode (211 $cm^{-1}$), respectively [25]. Moreover, all the Raman peaks of $BiVO_4$/$MoO_x$ shift to lower frequencies with the increase of $MoO_x$ loading were compared with pure $BiVO_4$, further indicating the presence of $MoO_x$ particles induces the crystal lattice distortion of $BiVO_4$.

Fig. S2a shows the $N_2$ adsorption-desorption isotherms of $BiVO_4$ photocatalyst with various $MoO_x$ contents. Type-II adsorption isotherms and a loop ring of type-H3 were observed across all materials, with no saturation adsorption platforms appearing. This suggests irregular pore structures in the samples [26]. The BET surface areas were determined to be 2.36, 2.07, 1.78, and 1.58 $m^2/g$ for $BiVO_4$, $BiVO_4$/0.05 $MoO_x$, $BiVO_4$/0.10 $MoO_x$, and $BiVO_4$/0.15 $MoO_x$, with mean pore sizes of 2.04, 1.94, 1.69 and 1.57 nm, respectively (Fig. S2b). The decrease in surface

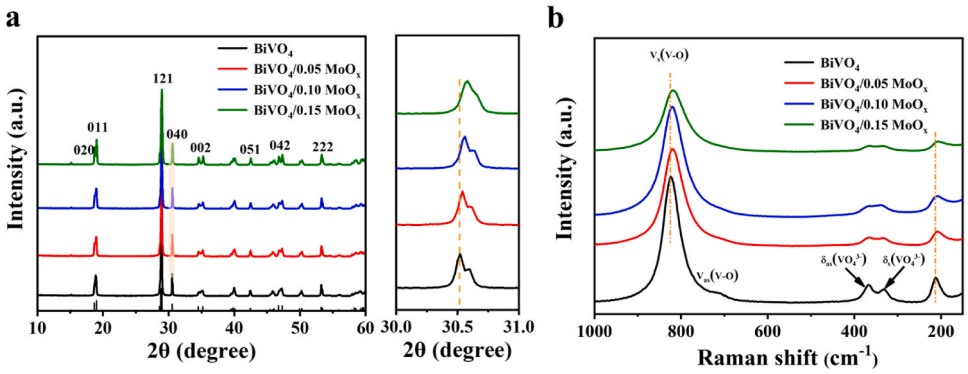


**Fig. 1.** XRD patterns (a) and Raman (b) spectra of $BiVO_4$, $BiVO_4$/0.05 $MoO_x$, $BiVO_4$/0.10 $MoO_x$ and $BiVO_4$/0.15 $MoO_x$.

area and mean pore size is attributed to the deposition of $MoO_x$. Fig. 2a-d show the transmission electron microscopy (TEM) and high-resolution transmission electron microscopy (HR-TEM) images of $BiVO_4$ and $BiVO_4$/0.10 $MoO_x$. The pure $BiVO_4$ (Fig. 2a) exhibits a smooth surface, while the surface of $BiVO_4$/0.10 $MoO_x$ shows the presence of numerous nano-particles with a uniform size about 5 nm, as marked with red dotted circles (Fig. 2c). The lattice spacing of $BiVO_4$ 0.29 nm, which is corresponding to the (040) facet of $BiVO_4$. The lattice spacing of $MoO_x$ deposited on $BiVO_4$ (Fig. 2b and d) is 0.32 and 0.34 nm, corresponding to the (210) and (040) facet of $MoO_3$, respectively [22,27–29]. Furthermore, energy-dispersive spectroscopy (EDS) mapping analysis (Fig. 2e) verifies the homogeneous distribution of Bi, V, O, and Mo elements in $BiVO_4$/0.10 $MoO_x$ [30]. Additionally, the Mo element contents in $BiVO_4$/0.05 $MoO_x$, $BiVO_4$/0.10 $MoO_x$, and $BiVO_4$/0.15 $MoO_x$ were determined to be 0.06 wt%, 0.10 wt%, and 0.16 wt% respectively, using inductively coupled plasma optical emission spectrometry (ICP-OES).

X-ray photoelectron spectroscopy (XPS) was used to deeply analyze the electronic structures of as prepared photocatalysts. The overall XPS survey spectrum (Fig. 3a) indicates the existence of Bi, V, O and Mo elements on the surface of $BiVO_4$/0.10 $MoO_x$, which is in good agreement with the result of EDS mapping. As depicted in Fig. 3b, the O1s spectrum of pure $BiVO_4$ presents three peaks appearing at 529.37, 531.04, and 532.94 eV, which are attributed to the Bi–O, V–O, and C═O, respectively [31,32]. Meanwhile, $BiVO_4$/0.10 $MoO_x$ shows an additional peak at 531.75 eV, which belongs to the O element in the vicinity of the oxygen vacancy ($V_O$) [33]. As presented in Fig. 3c, peaks at binding energies of 233.01 and 234.77 eV are attributed to the $3d_{3/2}$ and $3d_{5/2}$ orbitals of $Mo^{6+}$, respectively [34]. Besides, peaks at binding energies of 229.00 and 231.11 eV are attributed to the $3d_{3/2}$ and $3d_{5/2}$ orbitals of $Mo^{5+}$, respectively. Meanwhile, the EPR signal (Fig. S4 a) of $BiVO_4$/0.10 $MoO_x$ can be attributed to $Mo^{5+}$ and $V_O$ induced by $Mo^{5+}$ with the g factors of 1.899 and 2.003, respectively [35]. The V 2p spectrum is shown in Fig. 3d. It is noted that two new peaks appear at the binding energies of 518.19 and 524.96 eV, which are respectively attributed to the $2p_{3/2}$ and $2p_{1/2}$ orbitals of V element with V–O–Mo bonds [25,36]. Furthermore, the binding energy of Bi 4f in $BiVO_4$/$MoO_x$ is higher than that of pure $BiVO_4$, suggesting that electrons flow from $BiVO_4$ into $MoO_x$. (Fig. S4 b). All the above results demonstrate that $MoO_x$ is well decorated on the surface of $BiVO_4$.

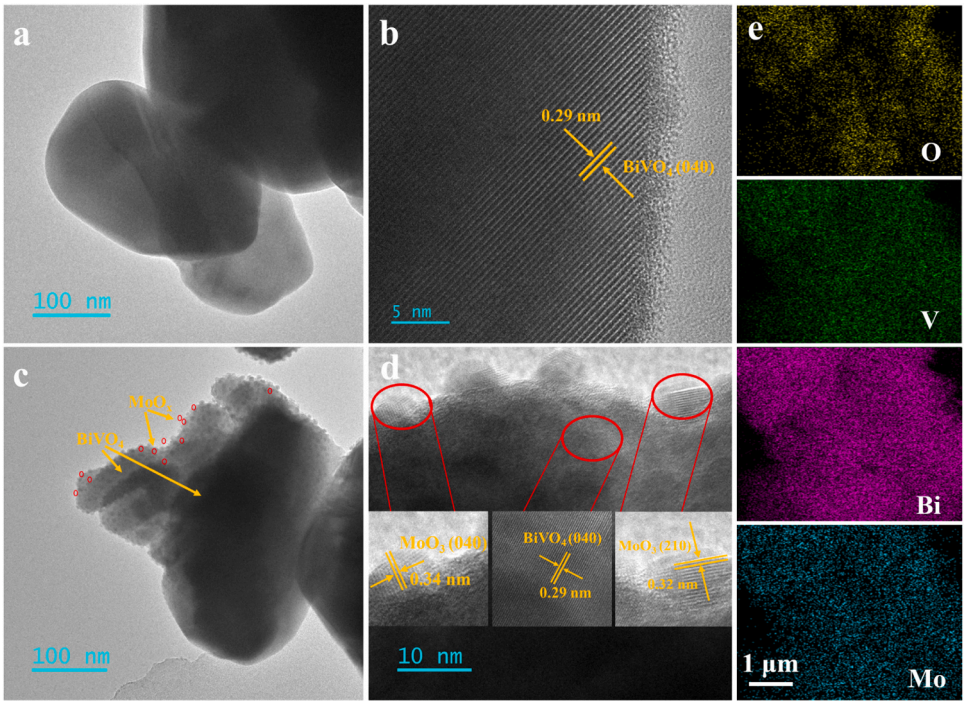


**Fig. 2.** TEM image of $BiVO_4$ (a)-(b) and $MoO_x$-$BiVO_4$ (c)-(d); (e) Elemental mapping images of $BiVO_4$/ 0.10 $MoO_x$.

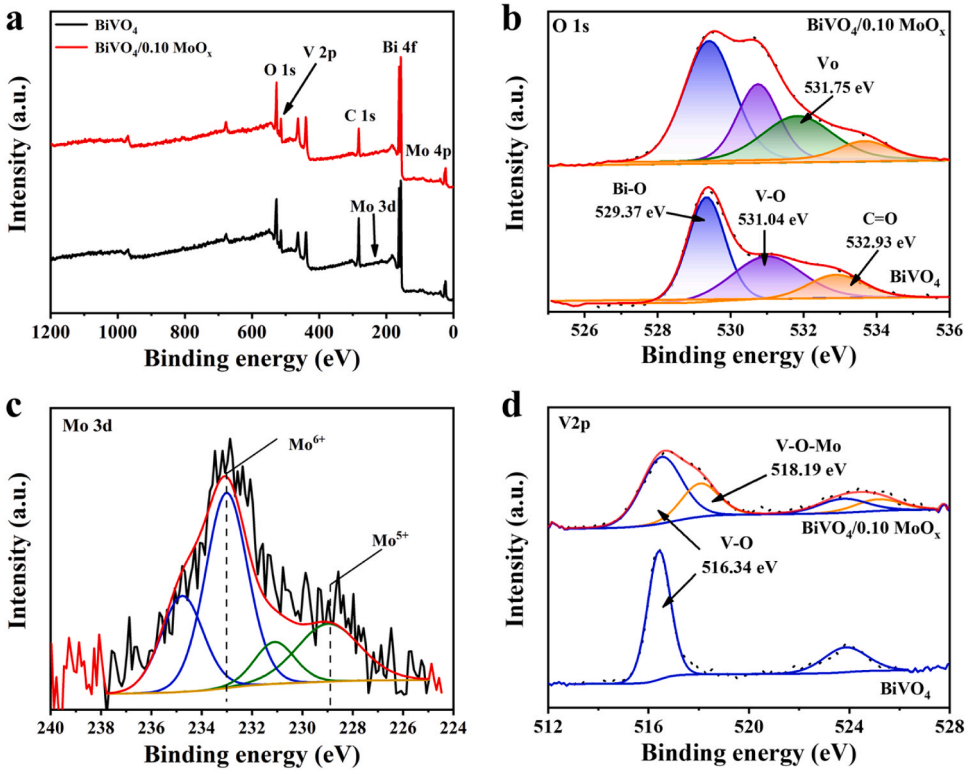


**Fig. 3.** XPS spectra of $BiVO_4$ and $BiVO_4$/0.10 $MoO_x$: (a) Survey, (b) O 1 s, (c) Mo 3d and (d) V 2p.

### *3.2. Evaluation of optical properties of $BiVO_4/MoO_x$ photocatalyst*

The optical properties of $BiVO_4$ and $BiVO_4/MoO_x$ composites were evaluated using UV–vis diffuse reflectance spectroscopy (DRS). As shown in Fig. 4a, the optical absorption of $BiVO_4/MoO_x$ is slightly enhanced as the load of $MoO_x$ increases, expanding the absorption in the wavelength range from 350 to 800 nm. Accordingly, the indirect band gap of $BiVO_4$ is 2.43 eV, calculated by the Kubelka-Munk method (Fig. S5), which is consistent with what previously reported [37]. The valence band potential (VB) of pure $BiVO_4$ was determined using ultraviolet photoelectron spectroscopy (UPS) by subtracting the difference between fermi edge and cut-off edge from the initial energy (21.22 eV), resulting in a value of 6.76 eV [38]. Moreover, the conduction band position is estimated to be 4.33 eV by subtracting the band gap (Eg) from the valence band potential (Fig. S6). In order to convert these values from electron volts to electrochemical energy potentials in volts, a reference standard is used where 0 V versus a normal hydrogen electrode (NHE, pH = 7) is equivalent to –4.44 V versus the vacuum level. Hence, the $E_{CB}$ and $E_{VB}$ of $BiVO_4$ are –0.11 and 2.32 V, respectively (vs NHE pH = 7), with a suitable electronic band structure to oxidize PET hydrolysate and reduce $H_2O$ into $H_2$, simultaneously.

As is known, the separation efficiency of photogenerated charge carriers in a catalyst is crucial to its photocatalytic performance [39,40]. Considering this, the steady-state photoluminescence (PL) spectra were collected to assess the separation efficiency of the photogenerated electron-hole pairs. As displayed in Fig. 4b, all the samples exhibit an emission peak around 580 nm, and the PL intensity significantly diminishes after the addition of $MoO_x$ onto $BiVO_4$. Among them, the $BiVO_4$/0.10 $MoO_x$ exhibits the weakest PL peak, indicating the highest efficiency in separating photogenerated charge carriers.

Meanwhile, transient photocurrent (PC) of all samples were measured under a 300 W Xe lamp (Fig. 4c), and the current density was enhanced after decorating $BiVO_4$ with $MoO_x$. Among all the samples, $BiVO_4$/0.10 $MoO_x$ exhibits the highest photocurrent density, indicating a superior photoinduced charge-carrier separation efficiency. Besides, electrochemical impedance spectroscopy (EIS) study was conducted to evaluate the behavior of charge carriers' migration. As presented in Fig. S7, it is evident that the capacitance arc for $BiVO_4$/0.10 $MoO_x$ is smaller compared to other samples. This observation indicates that the electron mobility of $BiVO_4$/0.10 $MoO_x$ has been enhanced, and the recombination of electron-hole pairs has been effectively suppressed following the decoration of $MoO_x$ on $BiVO_4$. Generally, efficient separation of charge carriers also results in an increase in carrier lifetime. To demonstrate this, transient fluorescence spectra for the $BiVO_4$ $BiVO_4$/0.05 $MoO_x$, $BiVO_4$/0.10 $MoO_x$ and $BiVO_4$/0.15 $MoO_x$ were performed, and their average fluorescence lifetimes were derived to be 4.26, 5.67, 12.41, and 8.38 ns, respectively (Fig. 4d). The lifetimes of carriers were significantly enhanced, indicating that the $MoO_x$ nano-particles effectively promote the separation of photogenerated carriers in $BiVO_4$.

The separation of charge carriers over the photocatalyst is a prerequisite for photocatalysis rection; however, sufficient active sites on the catalyst to manipulate electrons to result in efficient reduction is equally important. Based on linear sweep voltammetry (LSV) curves testing, the onset potential is positively shifted when decorating $MoO_x$ nano-particles onto $BiVO_4$, due to the co-catalytic effect of $MoO_x$ (Fig. 4e). Additionally, $BiVO_4$/0.10 $MoO_x$ exhibits the highest hydrogen evolution reaction (HER) activity among all $BiVO_4/MoO_x$ catalysts. Moreover, the promoted HER activity was understood by DFT calculations (Fig. 4f and S8). Compared to pure $BiVO_4$, the $BiVO_4$/0.10 $MoO_x$ exhibits more advantageous interactions with the H* intermediates, primarily due to the change in coordination number of surface oxygen atoms from 2 to 1. Therefore, the decoration of $MoO_x$ is beneficial for boosting the $H_2$ evolution of the photocatalyst.

Surface photovoltage spectroscopy (SPV) was employed to investigate the dynamic behaviors of the photogenerated electron-hole pairs in both prepared $BiVO_4$ and $BiVO_4$/0.10 $MoO_x$. As shown in Fig. 4g, both $BiVO_4$ and $BiVO_4$/0.10 $MoO_x$ present an intense SPV response region in the wavelength range from 300 to 520 nm, attributed to the band-to-band transition. The band-to-band transition of $BiVO_4$ is constructed by two processes: response in the UV region and visible light region,

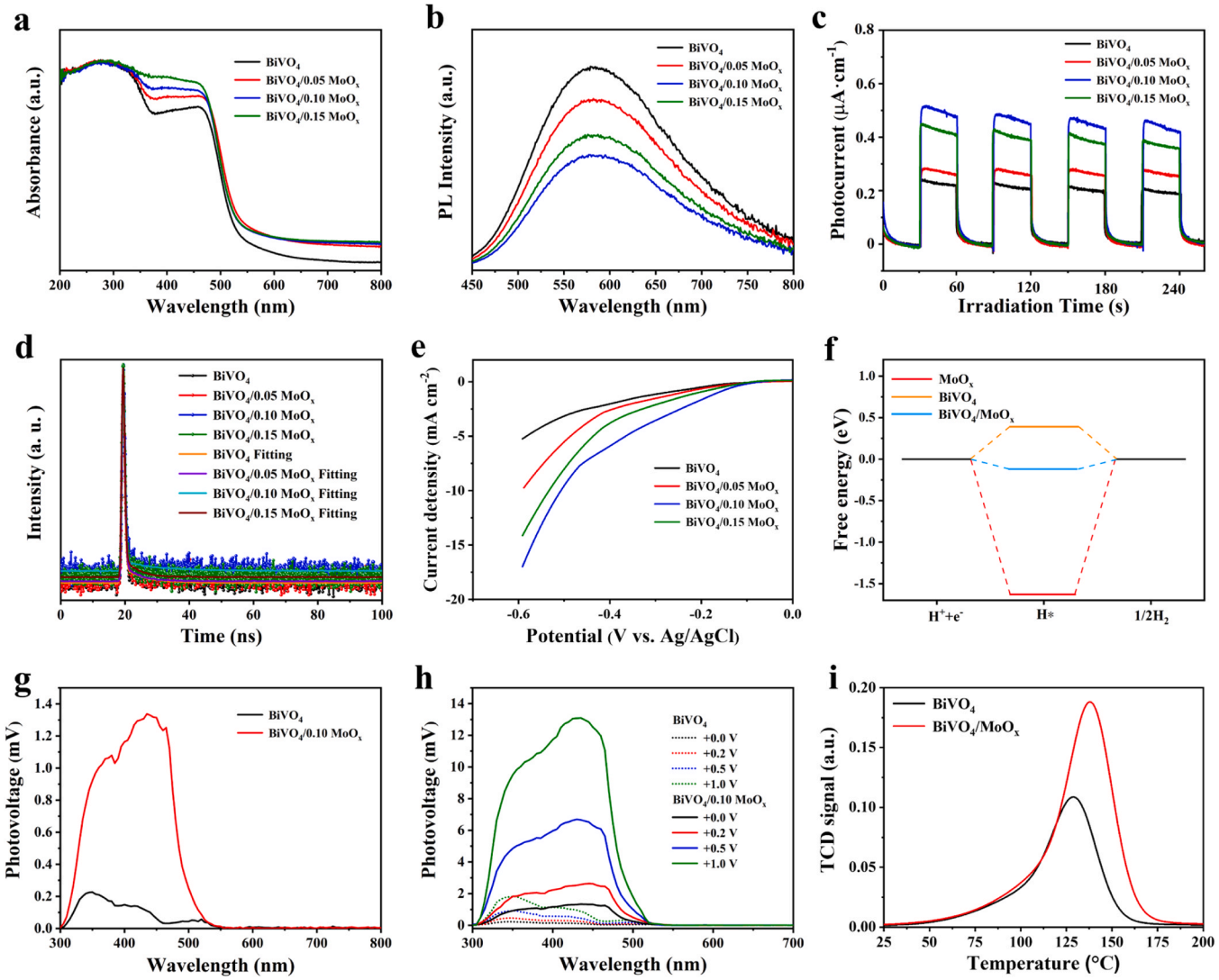


**Fig. 4.** (a) UV–vis DRS spectra, (b) fluorescence spectra, (c) photocurrents, (d) PL decay traces, (e) Linear sweep voltammetry (LSV) curves of the $BiVO_4/MoO_x$ photocatalysts. (f) Computed free-energy diagram for HER on $BiVO_4$ and $BiVO_4/MoO_x$. (g) Surface photovoltage spectra, (h) the field-induced surface photovoltage spectra under different external electric fields, and (i) $H_2O$-TPD for pure $BiVO_4$ and $BiVO_4$/0.10 $MoO_x$.

which are attributed to the band transition from O 2p and the hybrid orbital of Bi 6s and O 2p to V 3d orbital, respectively [41]. The stronger SPV intensity observed in $BiVO_4$/0.10 $MoO_x$ indicates that the decoration of $MoO_x$ nano-particles enhances the separation efficiency of photogenerated electron-hole pairs.

Moreover, field induced surface photovoltage spectra (FISPS) to investigate the influence of polarization effect [42]. As shown in Fig. 4h, the SPV response intensities for both $BiVO_4$ and $BiVO_4$/0.10 $MoO_x$ increase with the increase positive electric field, suggesting that the direction of external field and polarization electric field in $BiVO_4$ are consistent. More importantly, $BiVO_4$/0.10 $MoO_x$ exhibits higher SPV intensities in the response region (300–520 nm) than pure $BiVO_4$ at the same external voltage, suggesting that the $V_o$ in $MoO_x$ enhances the polarization effect of $BiVO_4$. Furthermore, the electric hysteresis loops for as-prepared samples were conducted to reveal the ferroelectric performance and the polarization electric field is mainly contributed by $P_r$ after the corona poling. As illustrated in Fig. S9, the values of $P_r$ were found to be 0.45 and 0.54 $\mu C \cdot cm^{-2}$ for $BiVO_4$ and $BiVO_4$/0.10 $MoO_x$, respectively. The improved ferroelectric polarization can be attributed to the $V_o$ in $MoO_x$ of $BiVO_4$/0.10 $MoO_x$, which is consistent with FISPS results.

The interaction between reactant molecules and catalysts was characterized through contact angle measurements of pretreated PET and temperature-programmed $H_2O$ desorption ($H_2O$-TPD). The $BiVO_4$/0.10 $MoO_x$ exhibits stronger surface hydrophilicity compared to pure $BiVO_4$ (Fig. S10). Besides, the peaks of $H_2O$ in the cases of $BiVO_4$ and $BiVO_4$/0.10 $MoO_x$ locate at 128 and 138 °C, respectively (Fig. 4i), indicating the favorable adsorption of $H_2O$ with the introduction of $MoO_x$, consistent with the contact angle measurements. In summary, on $BiVO_4$/0.10 $MoO_x$ exhibited a more profound polarization effect, leading to enhanced adsorption and activation of the pretreated PET, which is beneficial for its oxidation.

### 3.3. *Photoreforming of pretreated PET*

Due to the insolubility of the PET substrate, it was pretreated in a 1 M KOH solution to initiate the decomposition of the polymer (ethylene glycol and terephthalate) before photoreforming (Fig. S11). Quantitative 1 H nuclear magnetic resonance (NMR) spectroscopy shows that 37 % of ethylene glycol (EG) and 33 % of terephthalic acid (TPA) in PET were released with 2 mmol $L^{-1}$ of maleic acid as the standard (Table S1 and Fig. 5a). After 5 h photoreforming, three carboxylate products were detected from the pretreated PET, identified as formate, acetate, and a trace of glycolate. Besides, the concentration of EG monomers decreased

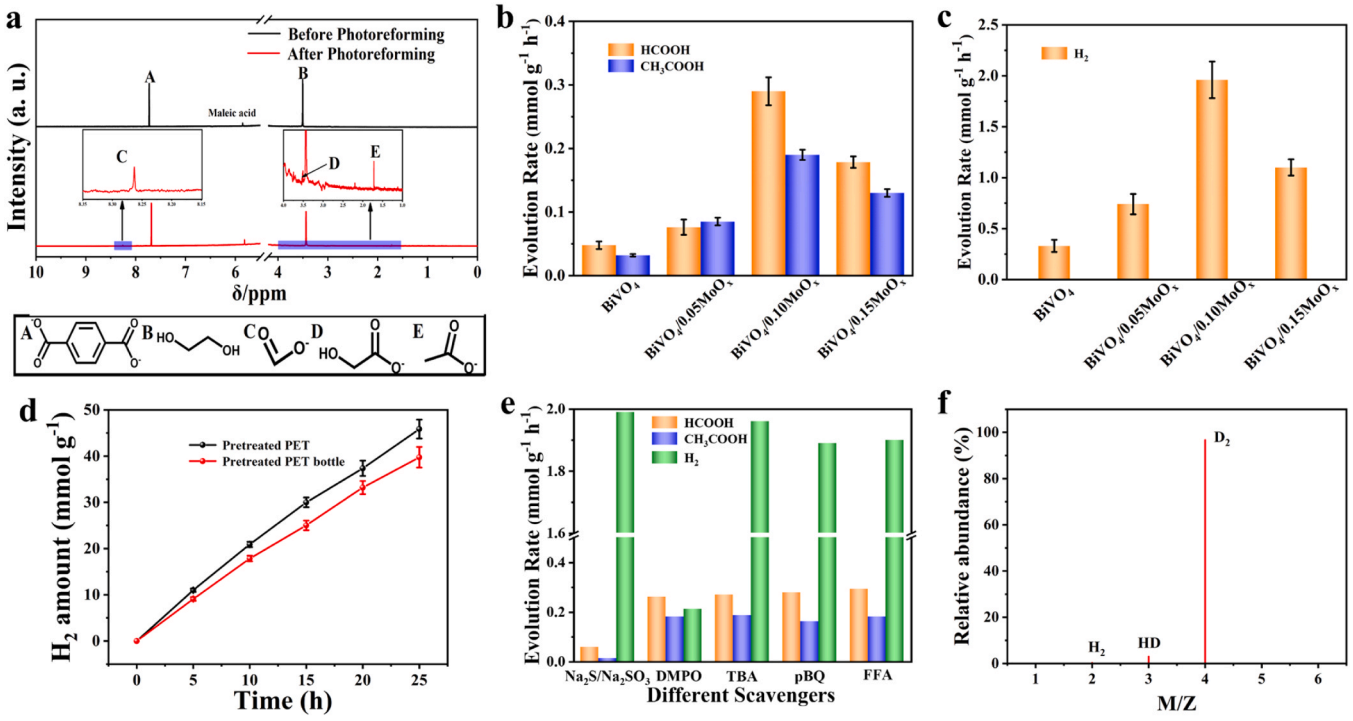


**Fig. 5.** $^1$H NMR spectra of photoreforming the pretreated PET for 5 h; insets are the partial enlarged of the spectra marked by a blue color. A, B, C, D and E correspond to TPA, EG, formate, acetate and glycolate. (b) The evolution rate of formate, acetate and (c) $H_2$ during photoreforming PET process for 5 h. (d) $H_2$ yield in the process of photoreforming pretreated PET and PET bottle in 25 h. (e) Control experiments with different scavengers. (f) MS spectrum of PET photoreforming over $BiVO_4$/0.10 $MoO_x$ with $D_2O$ and NaOD as hydrogen sources. Reaction conditions: 0.2 g PET powder was added into 10 mL $D_2O$ with 1 M NaOD followed by the photoreforming tests (5 h) over $BiVO_4$/0.10 $MoO_x$ (50 mg).

from 32.2 to 28.6 mmol $L^{-1}$ with photoreforming (Fig. 5a), whereas the concentration (from 28.8 to 28.7 mmol $L^{-1}$) of TPA monomers presented no significant change. This indicates that all the products were converted through the oxidation of the EG component of PET rather than TPA, and the conversion of EG was calculated to be 11.2 %.

Moreover, all liquid products were further quantified by HPLC. The formate generation rates of $BiVO_4$, $BiVO_4$/0.05 $MoO_x$, $BiVO_4$/0.10 $MoO_x$, and $BiVO_4$/0.15 $MoO_x$ were determined to be 0.047, 0.076, 0.29, and 0.18 mmol $g^{-1}$ $h^{-1}$ after 5 h of irradiation. Meanwhile, the acetate generation rates were calculated to be 0.032, 0.085, 0.19, and 0.13 mmol $g^{-1}$ $h^{-1}$, respectively (Fig. 5b and Fig. S12). Besides, the reduction half-reaction over $BiVO_4$, $BiVO_4$/0.05 $MoO_x$, $BiVO_4$/0.10 $MoO_x$, and $BiVO_4$/0.15 $MoO_x$ was quantified by gas chromatograph (GC). Typically, the $H_2$ evolution rates of all the samples were 0.33, 0.74, 1.96, and 1.10 mmol $g^{-1}$ $h^{-1}$ in the 5 h photoreforming (Fig. 5c), indicating efficient PET photoreforming performance in non-toxic photocatalysts (Table S2). Clearly, the $BiVO_4$/0.10 $MoO_x$ presents the highest activity in the reduction half-reaction, which is consistent with the results of the oxidation half-reaction. As displayed in Fig. 5d, $BiVO_4$/0.10 $MoO_x$ exhibits stable $H_2$ evolution over 25 h of PET photoreforming, with an average activity of 1.8 ± 0.08 mmol $g^{-1}$ $h^{-1}$. Moreover, the morphology and crystal structure of $BiVO_4$/0.10 $MoO_x$ are retained after photoreforming (Fig. S13), indicating its good durability. In order to identify the active species, various scavengers (i.e., $Na_2S$/$Na_2SO_3$, DMPO, tert-Butanol (TBA), p-Benzoquinone (p-BQ) and furfuryl alcohol (FFA) as hole, •H radical, •OH radical, $•O_2^-$ radical and $^1O_2$ scavengers, respectively) were added during the pretreated PET photoreforming process (Fig. 5e). Subsequently, the yield of formate and acetate significantly decrease with the addition of 0.05 M $Na_2S$/$Na_2SO_3$, while there is no clear change with the addition of other scavengers, suggesting that photogenerated holes play the major role in EG oxidation. Interestingly, the yield of $H_2$ decreases with the addition of 0.05 M DMPO, demonstrating that certain kind of free radicals, which are generated through the reduction of electrons, participate in $H_2$ production. The origin of evolving $H_2$ was analyzed by the $D_2O$ isotope-labeling experiment. The detected mass-spectrometry signals at $m/z$ = 2, 3 and 4 are attributed to the $H_2$, HD and $D_2$, strongly indicating the $H_2$ product is derived from $H_2O$ rather than PET (Fig. 5f). Additionally, $CO_3^{2-}$ was formed as a side product through further oxidation of formate, and its concentration was quantified by a previously reported method with an accumulation of 0.062 mmol (Fig. S14) [43]. After 5 h of photoreforming of pretreated PET, 0.0725 mmol of formate, 0.0475 mmol of acetate, and 0.062 mmol of $CO_3^{2-}$ were generated. The selectivity of the main products was evaluated to be 20.1 %, 26.4 % and 17.3 %, respectively (Table S3). The carbon balance of these products is approximately 63.8 %, which could be attributed to the fact that a few side products were not detected using $^1$H NMR and HPLC. Moreover, to pave the way for the industrialization of photoreforming plastic, a typical real-world photoreforming experiment was conducted. As shown in Fig. 5d, when PET bottles were pretreated as feedstocks, the average $H_2$ generation rate is determined to be 1.6 ± 0.09 mmol $g^{-1}$ $h^{-1}$, which is close to that of PET powder photoreforming. Therefore, this technology displays positive versatility and scalability for utilizing photocatalysis process to promote the upcycling of PET waste.

### 3.4. *Photoreforming mechanism*

To deeply understand the mechanism of PET photoreforming, we utilized in situ characterization techniques to identify the possible reaction intermediates. Considering that various free radicals may be involved in the process as important active species, in situ EPR was conducted to investigate the radical species in PET photoreforming. Meanwhile, due to the short lifetimes of radicals, 5,5-dimethyl-1pyrroline N-oxide (DMPO) was added as a spin trapping agent into the reaction solution. In Fig. 6a, it is shown that •H and •OH radicals can be trapped as a DMPO-H (hyperfine splitting constants, $A_N$ = 16.5 G, $A_H$ =

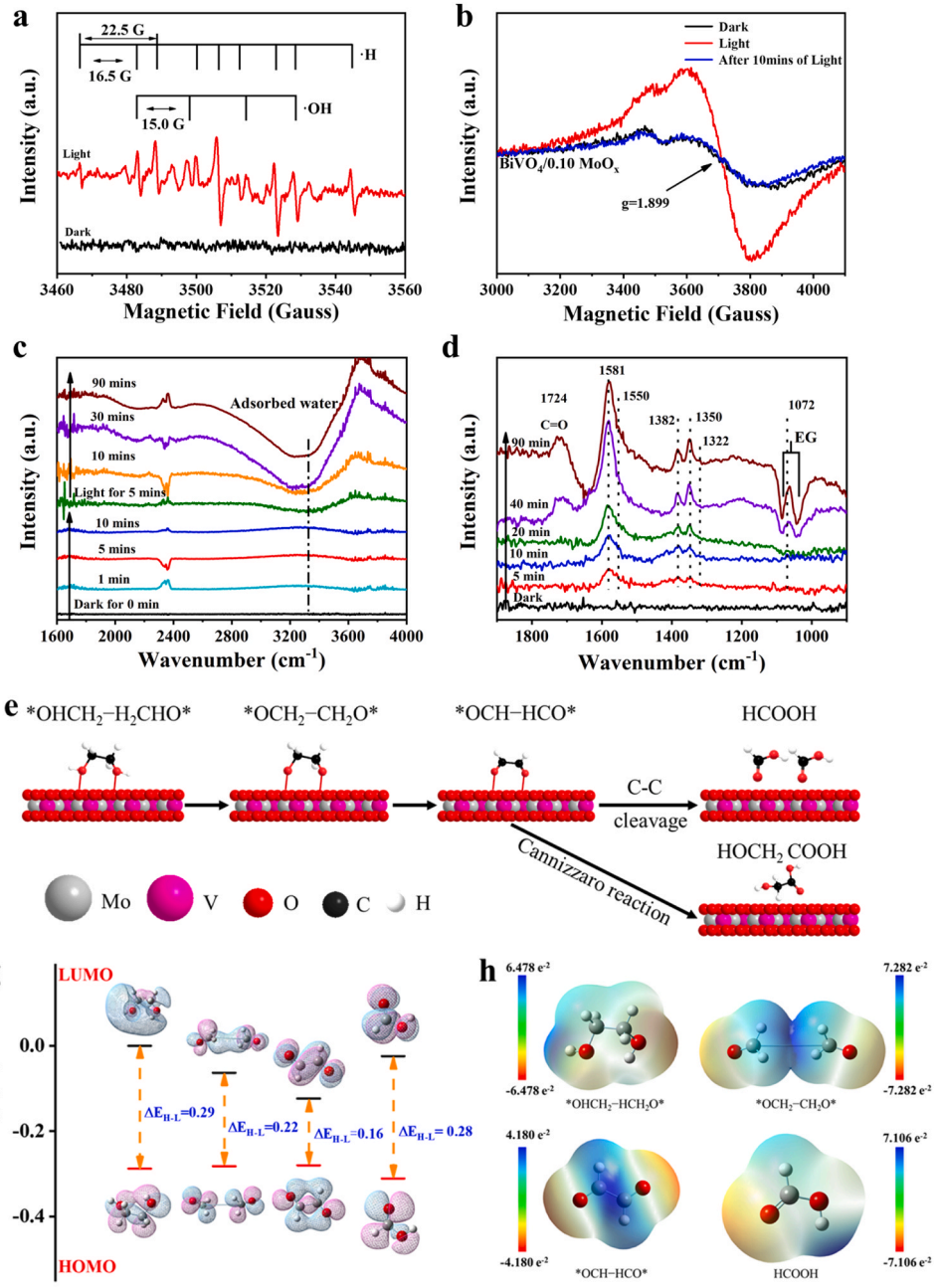


**Fig. 6.** (a) EPR spectra of •H and •OH radicals by using DMPO in 1.5 mL aqueous solution with dispersion of 5 mg $BiVO_4$/0.10 $MoO_x$. (b) Solid EPR spectra of $BiVO_4$/0.10 $MoO_x$ in dark condition, under light irradiation and after 10 mins of light. (c) In situ infrared spectra of $BiVO_4$/0.10 $MoO_x$. (d) In situ FTIR spectra of EG oxidation reaction on $BiVO_4$/0.10 $MoO_x$ in 1 M KOH. (e) The possible reaction pathways for the oxidation of EG to formic and glycolic acids. (f) The HOMO and LUMO electronic structures and gaps ($\Delta E_{H-L}$) of EG and its intermediates predicted by DFT calculations. (g) Electrostatic potential (ESP)-mapped molecular surface of EG and its intermediates.

22.5 G) and DMPO-OH ($A_N = 15.0$ G, $A_H = 14.8$ G) adducts over $BiVO_4$/0.10 $MoO_x$, whereas $\bullet O_2^-$ radicals were not observed (Fig. S15), demonstrating the generation of •H and •OH radicals during PET photoreforming processes [44,45]. Since the signal of •H radicals may interfere with the signal of •OH radicals, $Ag(NO_3)_3$ was employed as an electron sacrificial agent to prevent the generation of •H radicals. As a result, only the distinctive peak of •OH radicals emerged prominently (Fig. S16a). In order to explore the origin of •H and •OH radicals, EPR tests of pure $BiVO_4$ and $MoO_x$ were performed under the same conditions. As shown in Fig. S16b, no signals of •H radicals were detected for pure $MoO_x$ and $BiVO_4$, whereas pure $BiVO_4$ exhibited weak signals of •OH radicals. This suggests that the $MoO_x$ particles could act as a co-catalyst to enhance the production of •H radicals, thereby facilitating the $H_2$ evolution. During the process of PET photoreforming, the •OH radicals can be easily captured by TPA to generate TPA-OH. A characteristic PL peak of TPA-OH at 430 nm was observed (Fig. S17) [9], suggesting that •OH radicals hardly participate in the PET photoreforming process, which is consistent with the results of the control experiments. Moreover, the in situ solid EPR measurements of $BiVO_4$/0.10 $MoO_x$ were performed under different conditions. As shown in Fig. 6b, the EPR signal can be attributed to $Mo^{5+}$ and $V_o$ with the set of g factors of 1.899 and 2.003 [46]. It is worth noting that the EPR signal was enhanced under light condition, while it remained relatively unchanged after illumination, compared to the signal observed under dark

conditions. This observation suggests that the presence of $MoO_x$ nanoparticles serves as an intermediate medium for the capture and transfer of photogenerated electrons in $BiVO_4$. The electronic density of states of independent $BiVO_4$ and $MoO_x$ demonstrate that the conduction band minimum of $BiVO_4$ is higher than that of $MoO_x$ (Fig. S18). Therefore, it is thermodynamically feasible to transfer the photogenerated electrons from $BiVO_4$ to $MoO_x$. Additionally, $MoO_x$ can effectively activate the adsorbed water molecules as proved by in situ FTIR of $BiVO_4$/0.10 $MoO_x$ [47]. As displayed in Fig. 6c, the water gradually adsorbs to the surface of $BiVO_4$/0.10 $MoO_x$ and forms –OH groups at about 3330 $cm^{-1}$. Subsequently, the –OH groups disappear under light irradiation, suggesting the consumption of water. To sum up, the $MoO_x$ nano-particles can trap and transfer the photogenerated electrons from $BiVO_4$ to water, thereby promoting the generation of •H radicals and enhancing the performance of photocatalytic $H_2$ evolution.

Comparatively, the intermediates of the oxidation half-reaction were explored by in situ FTIR with an ATR method. Typically, to eliminate interference from TPA, pure EG was performed to reveal the mechanism of the PET photoreforming process. As shown in Fig. 6d, the FTIR peak at 1581 $cm^{-1}$ could be attributed to the C═O stretching vibration, while two peaks at 1382 and 1350 $cm^{-1}$ could be assigned to the $\delta$(–C–H) and the symmetric stretching vibration of O–C–O ($\nu s$(OCO)), indicating the generation of $HCOO^-$ [48,49]. Meanwhile, the peak at 1550 $cm^{-1}$ was because of the asymmetric stretching vibration of O–C–O, acetate. Based on the peak at 1581 $cm^{-1}$, glyoxal is one of the possible products, as the characteristic peak of glyoxal at 1071 $cm^{-1}$ also was observed. The simultaneous appearance of peaks at 1581 $cm^{-1}$, 1322 $cm^{-1}$, and 1072 $cm^{-1}$ suggests the potential production of glycolate species, which were also observed via $^1H$ NMR. Besides, the inverted peaks on both sides of 1072 $cm^{-1}$ are ascribed to the consumption of EG during photoreforming PET hydrolysate process, providing further evidence that the formate and acetate were transformed from EG. Therefore, the reaction pathway (Fig. 6e) for EG oxidation is proposed as follows: First, the EG molecules are adsorbed on the surface of $BiVO_4$ through bidentate configuration according to previous investigations; After that, the O–H bond cleavage occurs in EG to form the *$OCH_2$–$CH_2O$* intermediates; Finally, the *$OCH_2$–$CH_2O$* intermediates are converted into the *OCH–HCO* intermediates, and the *OCH–HCO* intermediates are oxidized to generate formic acid. Besides, glyoxal could be converted to glycolic acid by the Cannizzaro reaction in an alkaline solution.

To investigate the rationality of the reaction pathways, the impact of functional groups of EG and its intermediates were analyzed based on the orbital structures. From the HOMO and LUMO electronic structure diagrams in Fig. 6f, the functional groups of –OH, –O–, HC═O and –COOH have an obvious effect on electronic structures of HOMO and LUMO for EG and its intermediates. As displayed in Fig. 6f, the aldehyde groups in *OCH–HCO* intermediates impact HOMO-LUMO gap more than other intermediates with the lower $\Delta E_{H\text{-}L}$ = 0.16 eV which indicates that this compound has more ability to react with water molecule to form other products in solution. Also, for *$OCH_2$–$CH_2O$* intermediates with $\Delta E_{H\text{-}L}$ = 0.22 eV, the presence of peroxide substitution induces a clear impact on HOMO-LUMO gap higher than HCOOH with $\Delta E_{H\text{-}L}$ = 0.28 eV close to the initial product EG, which indicates that *$OCH_2$–$CH_2O$* is more reactive than HCOOH. In summary, the effect of groups substitution in the process of PET photoreforming induces a large reduction in the HOMO-LUMO gap, thus the intermediate reacts easily to generate formic acid [50].

Furthermore, an analysis was conducted on the distribution of electrostatic potential (ESP) on the surface of the EG molecule and its intermediates (Fig. 6g). The electrostatic potential is found to be more negative around the region surrounding of oxygen groups atoms for EG and its intermediates, suggesting that the positions may be subject to electrophilic attack. From the electrostatic potential results, it is understandable that all the obtained intermediates show high reactivity compared to EG. However, the absolute ESP value of HCOOH is much greater than that of *OCH–HCO* intermediate, indicating that the reaction from *OCH–HCO* intermediate to HCOOH is difficult to occur, due to the fact that the C–C bond cleavage of glyoxal intermediates is an endothermic process. Therefore, the cleavage of C–C bond is the rate-determining step during EG oxidation process [51].

According to the above results, the mechanism of the photoreforming pretreated PET into $H_2$ and formate over $BiVO_4$/$MoO_x$ can be divided into reduction and oxidation reactions, in which the EG (hydrolyzed monomer of PET) underwent the photogenerated holes direct oxidative dehydrogenation and C–C bond cleavage to form formate over $BiVO_4$/$MoO_x$. Meanwhile, $MoO_x$ can trap and transfer the photogenerated electrons from $BiVO_4$ to promote $H_2$ evolution. Briefly, the overall photoreforming mechanism could be proposed as follows:

$$BiVO_4 \rightarrow e^- + h^+$$

Reduction reaction: $H_2O$ was reduced to $H_2$

$$e^- + Mo^{6+} \rightarrow Mo^{5+}$$

$$Mo^{5+} + H^+ \rightarrow Mo^{6+} + \bullet H \text{ (fast process)}$$

$$2\bullet H \rightarrow H_2\uparrow$$

Oxidation reaction: EG was oxidized into formate

$$CH_2OHCH_2OH_{sol} \rightarrow CH_2OHCH_2OH_{ads}$$

$$CH_2OHCH_2OH_{ads} + 2\,h^+ + 2OH^- \rightarrow *OCH_2\text{–}CH_2O* + 2\,H_2O$$

$$*OCH_2\text{–}CH_2O* + 2\,h^+ + 2OH^- \rightarrow *OCH\text{–}HCO* + 2\,H_2O$$

$$*OCH\text{–}HCO* + 2\,h^+ + 4OH^- \rightarrow 2HCOO^{-}* + 2\,H_2O$$

However, the acetate products do not appear in the proposed pathway as mentioned above. This may be due to the conversion of glycoaldehyde into acetaldehyde, followed by the oxidation of acetaldehyde into acetate [52]. Therefore, after 5 h of photoreforming of pretreated PET, 1.075 mmol of electrons ($e^-$) and 0.72 mmol of holes ($h^+$) were involved in the generation of various redox products (Table S2). The charge balance of these products was approximately 67 %, which could be attributed to that a few side products were not detected using $^1H$ NMR and HPLC [43].

## 4. Conclusion

In summary, $MoO_x$ nano-particles were employed as a non-noble cocatalyst and decorated onto $BiVO_4$, facilitating the photo-redox reactions of reforming PET. TEM and XPS measurements revealed the decoration of $MoO_x$ particles onto $BiVO_4$ through V–O–Mo bonds, resulting in the formation of nanoparticles sized about 5 nm. The oxygen vacancy ($O_v$) in $MoO_x$ particles promotes the adsorption of pretreated poly(ethylene-terephthalate) (PET), leading to enhanced oxidation of pretreated PET. Meanwhile, benefiting from the low conduction position and the variable valence of $Mo^{5+/6+}$ ions, $MoO_x$ can be regarded as an electron relay, facilitating the transfer of photogenerated electrons from $BiVO_4$ to $MoO_x$. As a result, the free energy of $H^+ + e^- \rightarrow H^*$ is lowered down from 0.39 to –0.12 eV, thus promoting the reduction of protons to produce $H_2$. Meanwhile, in-situ FTIR spectral results confirm that the possible reaction pathway of formate is achieved though the oxidation of EG on the surface of $BiVO_4$/$MoO_x$. In other words, a cooperative promotion of photo-redox was achieved in the process of PET photoreforming. The optimum activity of $BiVO_4$/$MoO_x$ for PET photoreforming into formate, acetate and $H_2$ are estimated to be 0.29, 0.19, and 1.96 mmol $g^{-1}$ $h^{-1}$, which are 6.2, 6.0, and 5.9 times higher than that of $BiVO_4$, respectively. The present work provides insights into designing highly efficient catalysts to achieve effective PET photoreforming into valuable chemicals accompanied by $H_2$ evolution under ambient condition.

## CRediT authorship contribution statement

**Fei Li:** Software, Investigation. **Feng Yu:** Software. **Abdelkader Labidi:** Software. **Eric Lichtfouse:** Writing – review & editing. **Xinxin Liang:** Writing – review & editing, Writing – original draft, Investigation, Data curation. **Ting Gao:** Formal analysis. **Chuanyi Wang:** Writing – review & editing, Funding acquisition, Conceptualization. **Ximing Li:** Investigation. **Yongqian Cui:** Investigation. **Qibing Dong:** Data curation.

## Declaration of Competing Interest

The authors declare that they have no known competing financial interests or personal relationships that could have appeared to influence the work reported in this paper.

## Data availability

The data that has been used is confidential.

## Acknowledgements

This work was supported by the National Natural Science Foundation of China (52161145409, 21976116), SAFEA of China ("Belt and Road" Innovative Talent Exchange Foreign Expert Project # 2023041004L) (High-end Foreign Expert Project # G2023041021L), and Alexander-von-Humboldt Foundation of Germany (Group-Linkage Program).

## Appendix A. Supporting information

Supplementary data associated with this article can be found in the online version at doi:10.1016/j.apcatb.2024.124326.

## References

[1] Q. Dong, A.D. Lele, X. Zhao, S. Li, S. Cheng, Y. Wang, M. Cui, M. Guo, A. H. Brozena, Y. Lin, T. Li, L. Xu, A. Qi, I.G. Kevrekidis, J. Mei, X. Pan, D. Liu, Y. Ju, L. Hu, Depolymerization of plastic by means of electrified spatiotemporal heating, Nature 616 (2023) 488–494.
[2] M. Chu, Y. Liu, X. Lou, Q. Zhang, J. Chen, Rational design of chemical catalysis for plastic recycling, ACS Catal. 12 (2022) 4659–4679.
[3] N.G. Posnack, Plastic and cardiovascular disease, Nat. Rev. Cardiol. 18 (2021) 69–70.
[4] L.D. Ellis, N.A. Rorrer, K.P. Sullivan, M. Otto, J.E. McGeehan, Y. Román-Leshkov, N. Wierckx, G.T. Beckham, Chemical and biological catalysis for plastic recycling and upcycling, Nat. Catal. 4 (2021) 539–556.
[5] X. Chen, Y. Wang, L. Zhang, Recent progress in the chemical upcycling of plastic wastes, ChemSusChem 14 (2021) 4137–4151.
[6] H. Zhou, Y. Wang, Y. Ren, Z. Li, X. Kong, M. Shao, H. Duan, Plastic waste valorization by leveraging multidisciplinary catalytic technologies, ACS Catal. 12 (2022) 9307–9324.
[7] K. Zheng, Y. Wu, Z. Hu, S. Wang, X. Jiao, J. Zhu, Y. Sun, Y. Xie, Progress and perspective for conversion of plastic wastes into valuable chemicals, Chem. Soc. Rev. 52 (2023) 8–29.
[8] S. Kang, T. Sun, Y. Ma, M. Du, M. Gong, C. Zhou, Y. Chai, B. Qiu, Artificial photosynthesis bringing new vigor into plastic wastes, SmartMat 4 (2023) e1202.
[9] T. Uekert, M.F. Kuehnel, D.W. Wakerley, E. Reisner, Plastic waste as a feedstock for solar-driven $H_2$ generation, Energ. Environ. Sci. 11 (2018) 2853–2857.
[10] T. Uekert, H. Kasap, E. Reisner, Photoreforming of nonrecyclable plastic waste over a carbon nitride/nickel phosphide catalyst, J. Am. Chem. Soc. 141 (2019) 15201–15210.
[11] S. Chu, B. Zhang, X. Zhao, H.S. Soo, F. Wang, R. Xiao, H. Zhang, Photocatalytic conversion of plastic waste: from photodegradation to photosynthesis, Adv. Energy Mater. 12 (2022) 2200435.
[12] J.H. Kim, J.S. Lee, Elaborately modified $BiVO_4$ photoanodes for solar water splitting, Adv. Mater. 31 (2019) 1806938.
[13] C. Li, P. Zhang, R. Lv, J. Lu, T. Wang, S. Wang, H. Wang, J. Gong, Selective deposition of $Ag_3PO_4$ on monoclinic BiVO4(040) for highly efficient photocatalysis, Small 9 (2013) 3951–3956.
[14] I. Chakraborty, T. Pradeep, Atomically precise particles of noble metals: emerging link between atoms and nanoparticles, Chem. Rev. 117 (2017) 8208–8271.
[15] J.-C. Liu, X.-L. Ma, Y. Li, Y.-G. Wang, H. Xiao, J. Li, Heterogeneous Fe3 single-particle catalyst for ammonia synthesis via an associative mechanism, Nat. Commun. 9 (2018) 1610.
[16] S. Ji, Y. Chen, Q. Fu, Y. Chen, J. Dong, W. Chen, Z. Li, Y. Wang, L. Gu, W. He, C. Chen, Q. Peng, Y. Huang, X. Duan, D. Wang, C. Draxl, Y. Li, Confined pyrolysis within metal–organic frameworks to form uniform Ru3 particles for efficient oxidation of alcohols, J. Am. Chem. Soc. 139 (2017) 9795–9798.
[17] C. Zhou, S. Wang, Z. Zhao, Z. Shi, S. Yan, Z. Zou, A facet-dependent schottky-junction electron shuttle in a $BiVO_4${010}–Au–$Cu_2O$ Z-scheme photocatalyst for efficient charge separation, Adv. Funct. Mater. 28 (2018) 1801214.
[18] G. Kresse, J. Furthmüller, Efficiency of ab-initio total energy calculations for metals and semiconductors using a plane-wave basis set, Comp. Mater. Sci. 6 (1996) 15–50.
[19] P.E. Blöchl, Projector augmented-wave method, Phys. Rev. B 50 (1994) 17953–17979.
[20] J.P. Perdew, K. Burke, M. Ernzerhof, Generalized gradient approximation made simple, Phys. Rev. Lett. 77 (1996) 3865–3868.
[21] S. Grimme, J. Antony, S. Ehrlich, H. Krieg, A consistent and accurate ab initio parametrization of density functional dispersion correction (DFT-D) for the 94 elements H-Pu, J. Chem. Phys. 132 (2010) 154104.
[22] R. Li, F. Zhang, D. Wang, J. Yang, M. Li, J. Zhu, X. Zhou, H. Han, C. Li, Spatial separation of photogenerated electrons and holes among {010} and {110} crystal facets of $BiVO_4$, Nat. Commun. 4 (2013) 1432.
[23] R.L. Frost, D.A. Henry, M.L. Weier, W. Martens, Raman spectroscopy of three polymorphs of $BiVO_4$: clinobisvanite, dreyerite and pucherite, with comparisons to $(VO_4)_3$-bearing minerals: namibite, pottsite and schumacherite, J. Raman Spectrosc. 37 (2006) 722–732.
[24] R. Kontic, G.R. Patzke, Synthetic trends for $BiVO_4$ photocatalysts: molybdenum substitution vs. $TiO_2$ and $SnO_2$ heterojunctions, J. Solid State Chem. 189 (2012) 38–48.
[25] Y. Wang, G. Tan, T. Liu, Y. Su, H. Ren, X. Zhang, A. Xia, L. Lv, Y. Liu, Photocatalytic properties of the g-$C_3N_4$/{010} facets $BiVO_4$ interface Z-Scheme photocatalysts induced by $BiVO_4$ surface heterojunction, Appl. Catal. B Environ. 234 (2018) 37–49.
[26] X. Liang, J. Zhao, T. Wang, Z. Zhang, M. Qu, C. Wang, Constructing a Z-scheme heterojunction photocatalyst of $GaPO_4$/α-MoC/$Ga_2O_3$ without mingling type-ii heterojunction for $CO_2$ reduction to CO, ACS Appl. Mater. Inter. 13 (2021) 33034–33044.
[27] G. Xi, J. Ye, Synthesis of bismuth vanadate nanoplates with exposed {001} facets and enhanced visible-light photocatalytic properties, Chem. Commun. 46 (2010) 1893–1895.
[28] C. Liu, H. Xu, Z. Chen, Q. Ye, X. Wu, J. Wang, B. Cao, Enhanced triethylamine sensing properties by designing an α-$Fe_2O_3$/α-$MoO_3$ nanostructure directly grown on ceramic tubes, ACS Appl. Nano Mater. 2 (2019) 6715–6725.
[29] J. Dong, Y. Shi, C. Huang, Q. Wu, T. Zeng, W. Yao, A new and stable Mo-$Mo_2C$ modified g-$C_3N_4$ photocatalyst for efficient visible light photocatalytic $H_2$ production, Appl. Catal. B Environ. 243 (2019) 27–35.
[30] X. Yang, L. Tian, X. Zhao, H. Tang, Q. Liu, G. Li, Interfacial optimization of g-$C_3N_4$-based Z-scheme heterojunction toward synergistic enhancement of solar-driven photocatalytic oxygen evolution, Appl. Catal. B Environ. 244 (2019) 240–249.
[31] Z. Pan, T. Hisatomi, Q. Wang, S. Chen, M. Nakabayashi, N. Shibata, C. Pan, T. Takata, M. Katayama, T. Minegishi, A. Kudo, K. Domen, Photocatalyst sheets composed of particulate $LaMg_{1/3}Ta_{2/3}O_2N$ and Mo-Doped $BiVO_4$ for Z-scheme water splitting under visible light, ACS Catal. 6 (2016) 7188–7196.
[32] S. Cao, B. Shen, T. Tong, J. Fu, J. Yu, 2D/2D heterojunction of ultrathin MXene/$Bi_2WO_6$ nanosheets for improved photocatalytic $CO_2$ reduction, Adv. Funct. Mater. 28 (2018) 1800136.
[33] R. Toyoshima, J. Kawai, K. Isegawa, H. Kondoh, A. Junkaew, A. Nakayama, T. Asano, M. Tamura, Y. Nakagawa, M. Yabushita, K. Tomishige, Detailed characterization of $MoO_x$-modified Rh metal particles by ambient-pressure XPS and DFT calculations, J. Phys. Chem. C 125 (2021) 4540–4549.
[34] W. He, Y. Wei, J. Xiong, Z. Tang, Y. Wang, X. Wang, H. Xu, X. Zhang, X. Yu, Z. Zhao, J. Liu, Variable valence $Mo^{5+}$/$Mo^{6+}$ ionic bridge in hollow spherical g-$C_3N_4$/$Bi_2MoO_6$ catalysts for promoting selective visible light-driven $CO_2$ photoreduction into CO, J. Energy Chem. 80 (2023) 361–372.
[35] Z. Shi, K. Nie, Z.-J. Shao, B. Gao, H. Lin, H. Zhang, B. Liu, Y. Wang, Y. Zhang, X. Sun, X.-M. Cao, P. Hu, Q. Gao, Y. Tang, Phosphorus-$Mo_2C$@carbon nanowires toward efficient electrochemical hydrogen evolution: composition, structural and electronic regulation, Energ. Environ. Sci. 10 (2017) 1262–1271.
[36] S.M. Thalluri, S. Hernández, S. Bensaid, G. Saracco, N. Russo, Green-synthesized W- and Mo-doped $BiVO_4$ oriented along the {040} facet with enhanced activity for the sun-driven water oxidation, Appl. Catal. B Environ. 180 (2016) 630–636.
[37] Z.-Y. Yu, C.-C. Lang, M.-R. Gao, Y. Chen, Q.-Q. Fu, Y. Duan, S.-H. Yu, Ni–Mo–O nanorod-derived composite catalysts for efficient alkaline water-to-hydrogen conversion via urea electrolysis, Energ. Environ. Sci. 11 (2018) 1890–1897.
[38] Z. Zhao, Z. Li, Z. Zou, Electronic structure and optical properties of monoclinic clinobisvanite $BiVO_4$, Phys. Chem. Chem. Phys. 13 (2011) 4746–4753.
[39] J. Liu, Y. Liu, N. Liu, Y. Han, X. Zhang, H. Huang, Y. Lifshitz, S.-T. Lee, J. Zhong, Z. Kang, Metal-free efficient photocatalyst for stable visible water splitting via a two-electron pathway, Science 347 (2015) 970–974.
[40] X. Li, Q. Dong, F. Li, Q. Zhu, Q. Tian, L. Tian, Y. Zhu, B. Pan, M. Padervand, C. Wang, Defective Bi@BiOBr/C microrods derived from Bi-MOF for efficient photocatalytic NO abatement: directional regulation of interfacial charge transfer via carbon–loading, Appl. Catal. B Environ. 340 (2024) 123238.
[41] A. Iwase, Y.H. Ng, Y. Ishiguro, A. Kudo, R. Amal, Reduced graphene oxide as a solid-state electron mediator in Z-scheme photocatalytic water splitting under visible light, J. Am. Chem. Soc. 133 (2011) 11054–11057.
[42] S. Gao, B. Gu, X. Jiao, Y. Sun, X. Zu, F. Yang, W. Zhu, C. Wang, Z. Feng, B. Ye, Y. Xie, Highly efficient and exceptionally durable $CO_2$ photoreduction to methanol

over freestanding defective single-unit-cell bismuth vanadate layers, J. Am. Chem. Soc. 139 (2017) 3438–3445.
[43] M. Du, Y. Zhang, S. Kang, X. Guo, Y. Ma, M. Xing, Y. Zhu, Y. Chai, B. Qiu, Trash to Treasure: photoreforming of plastic waste into commodity chemicals and hydrogen over $MoS_2$-tipped CdS nanorods, ACS Catal. 12 (2022) 12823–12832.
[44] S. Mu, H. Lu, Q. Wu, L. Li, R. Zhao, C. Long, C. Cui, Hydroxyl radicals dominate reoxidation of oxide-derived Cu in electrochemical $CO_2$ reduction, Nat. Commun. 13 (2022) 3694.
[45] K. Li, S. Ma, C. Zou, J. Latif, Y. Jiang, Z. Ni, S. Shen, J. Feng, H. Jia, Unrecognized role of organic acid in natural attenuation of pollutants by mackinawite (FeS): the significance of carbon-center free radicals, Environ. Sci. Technol. 57 (2023) 20871–20880.
[46] S. Feng, J. Zhao, Y. Bai, X. Liang, T. Wang, C. Wang, Facile synthesis of Mo-doped $TiO_2$ for selective photocatalytic $CO_2$ reduction to methane: Promoted $H_2O$ dissociation by Mo doping, J. $CO_2$ Util. 38 (2020) 1–9.
[47] H. Zhang, P. Zhang, M. Qiu, J. Dong, Y. Zhang, X.W. Lou, Ultrasmall $MoO_x$ particles as a novel cocatalyst for photocatalytic hydrogen evolution, Adv. Mater. 31 (2019) 1804883.
[48] J. Li, L. Li, X. Ma, X. Han, C. Xing, X. Qi, R. He, J. Arbiol, H. Pan, J. Zhao, J. Deng, Y. Zhang, Y. Yang, A. Cabot, Selective ethylene glycol oxidation to formate on nickel selenide with simultaneous evolution of hydrogen, Adv. Sci. 10 (2023) 2300841.
[49] S.C. Chang, Y. Ho, M.J. Weaver, Applications of real-time FTIR spectroscopy to the elucidation of complex electroorganic pathways: electrooxidation of ethylene glycol on gold, platinum, and nickel in alkaline solution, J. Am. Chem. Soc. 113 (1991) 9506–9513.
[50] D. Chen, H. Wang, HOMO–LUMO gaps of homogeneous polycyclic aromatic hydrocarbon particles, J. Phys. Chem. C 123 (2019) 27785–27793.
[51] J. Wang, X. Li, M. Wang, T. Zhang, X. Chai, J. Lu, T. Wang, Y. Zhao, D. Ma, Electrocatalytic valorization of poly(ethylene terephthalate) plastic and $CO_2$ for simultaneous production of formic acid, ACS Catal. 12 (2022) 6722–6728.
[52] A.J. Garza, A.T. Bell, M. Head-Gordon, Mechanism of $CO_2$ reduction at copper surfaces: pathways to C2 products, ACS Catal. 8 (2018) 1490–1499.

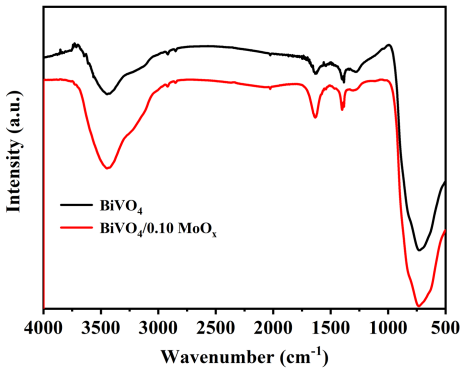


Figure S1 FTIR spectra of $BiVO_4$ and $BiVO_4$/0.10 $MoO_x$ photocatalysts.

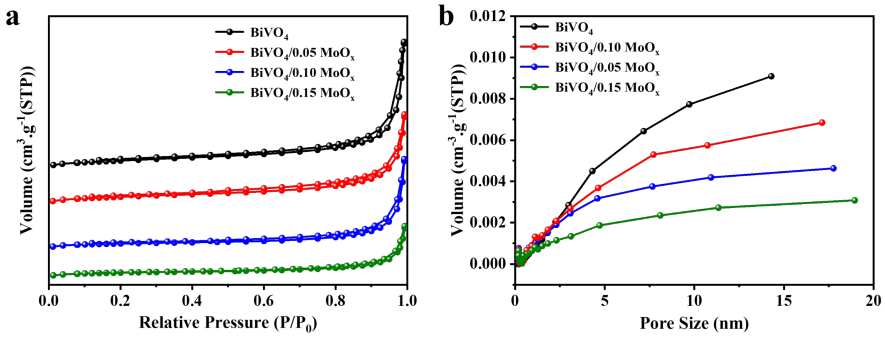


Figure S2 (a) The $N_2$ adsorption−desorption isotherms and (b) pore size distribution of $BiVO_4$, $BiVO_4$/0.05 $MoO_x$, $BiVO_4$/0.10 $MoO_x$ and $BiVO_4$/0.15 $MoO_x$.

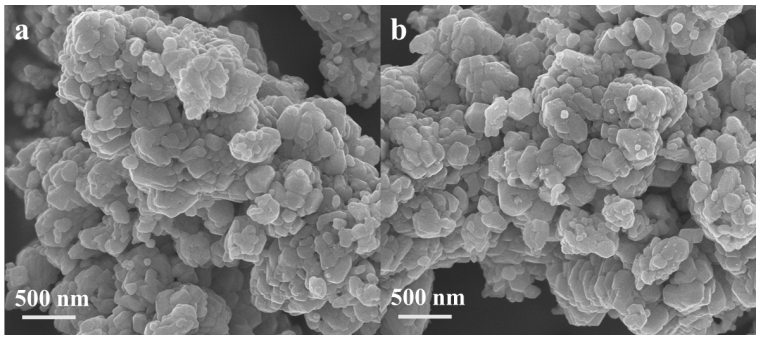


Figure S3 The SEM imagines of $BiVO_4$ and $BiVO_4$/0.10 $MoO_x$.

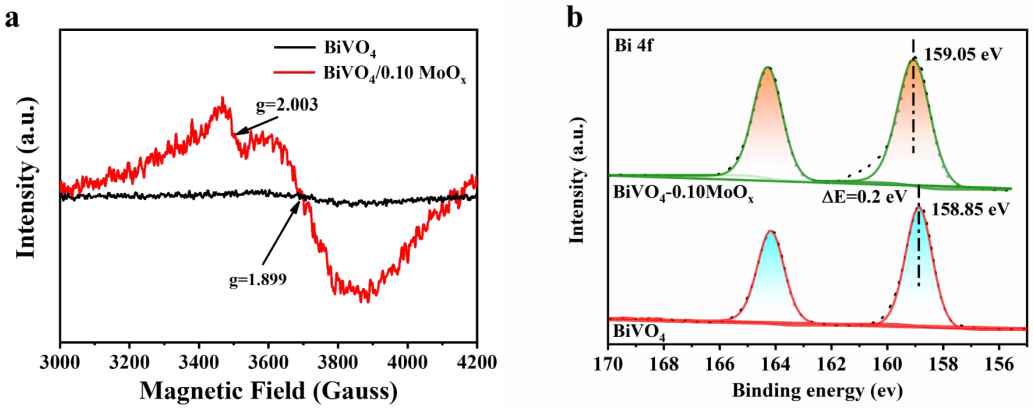


Figure S4 The EPR (a) and (b) XPS spectra of $BiVO_4$ and $BiVO_4$/0.10 $MoO_x$.

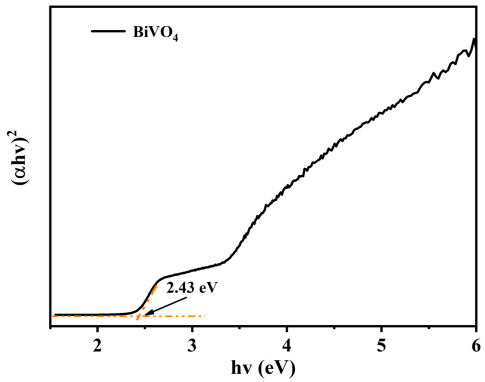


Figure S5. The $(\alpha h\nu)^2$ versus hν curves of $BiVO_4$.

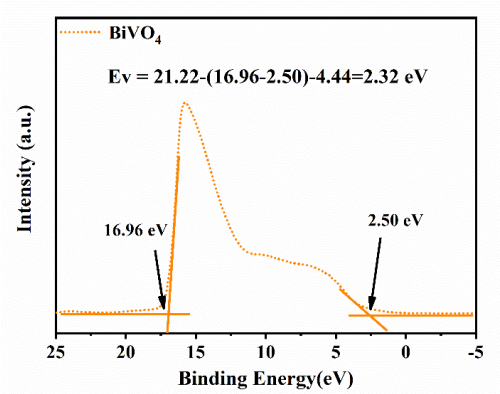


Figure S6. UPS spectra of $BiVO_4$.

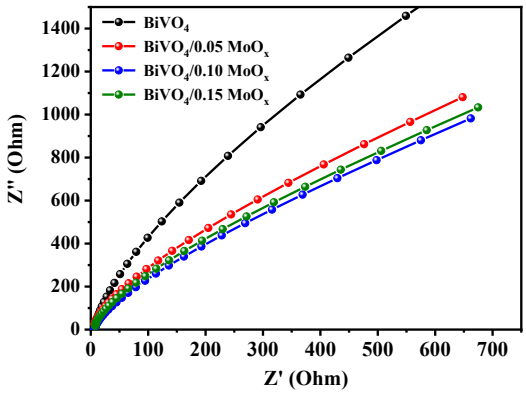


Figure S7. EIS Nyquist plots of $BiVO_4$.

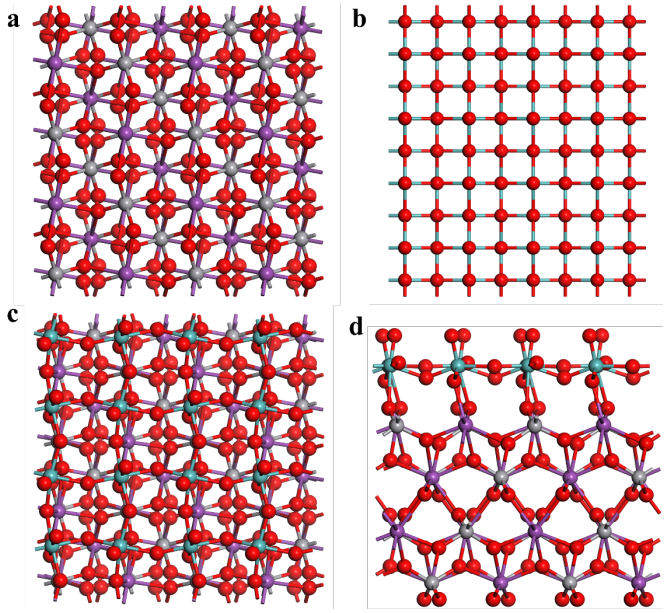


Figure S8. Atomic structure for (a) $BiVO_4$ crystal and (b) $MoO_x$ nano-clusters used for model construction. Grey-colour = V, purple = Bi, red = O and green = Mo. Computational model for interface structures of $BiVO_4/MoO_x$. (c) Side (elevation) and (d) Top (plan), view.

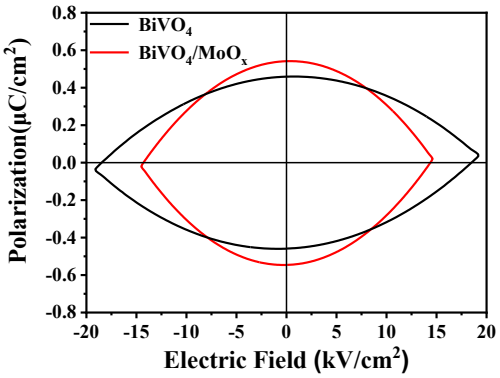


Figure S9. Electric hysteresis loop of $BiVO_4$ and $BiVO_4$/0.10 $MoO_x$.

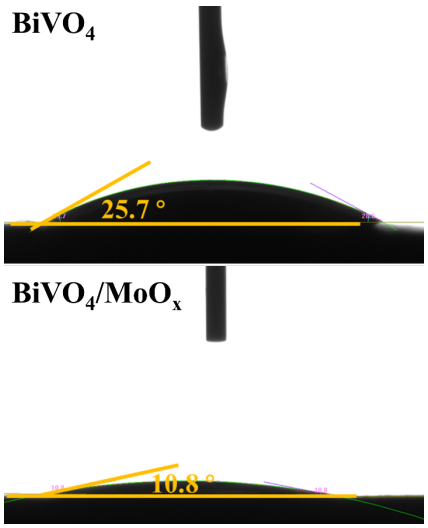


Figure S10. The pretreated contact angles of $BiVO_4$ and $BiVO_4$/0.10 $MoO_x$.

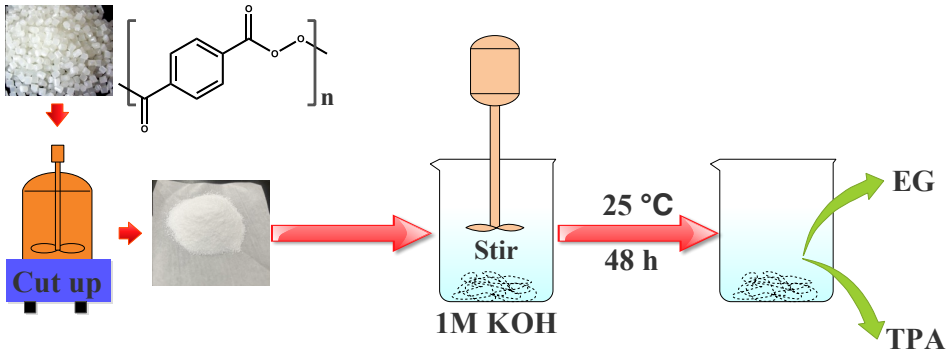


Figure S11. The processes of pretreated PET.

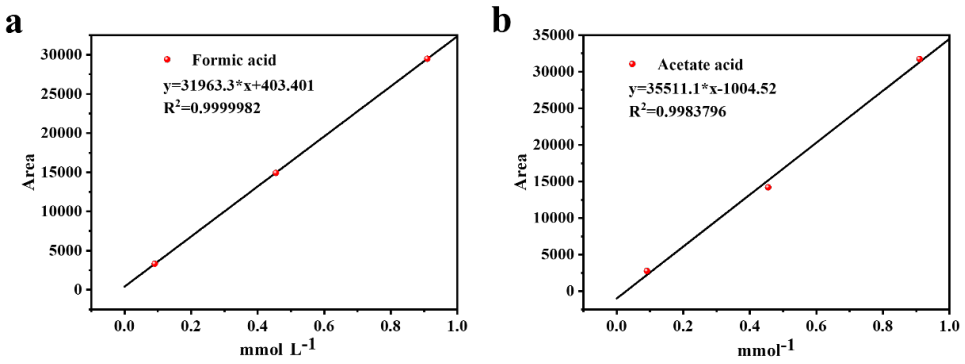


Figure S12. Calibration curves of formate (a) and acetic acid (b).

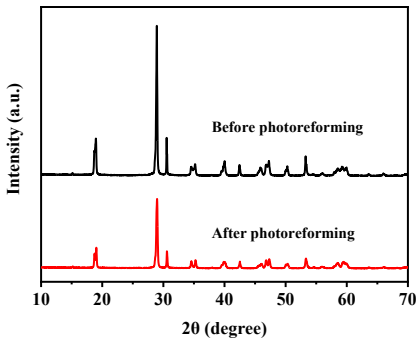


Figure S13. XRD pattern of $BiVO_4$/0.10 $MoO_x$ before and after photoreforming.

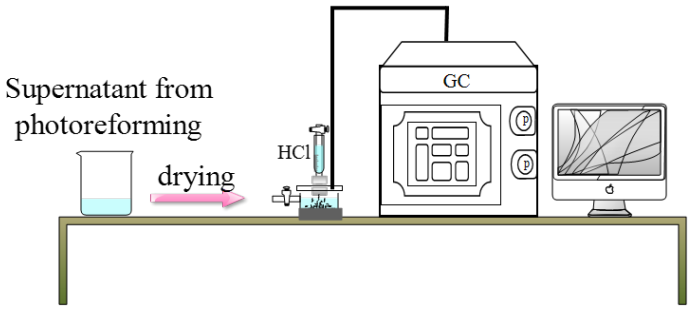


Figure S14. A self-built methodology for $CO_3^{2-}$ quantification.

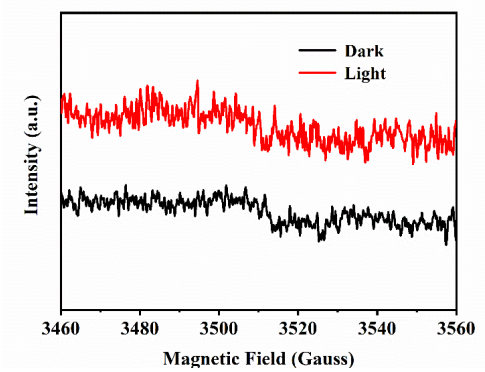


Figure S15. EPR spectra of $\bullet O_2^-$ radicals by using DMPO in an aqueous dispersion of $BiVO_4$/0.10 $MoO_x$.

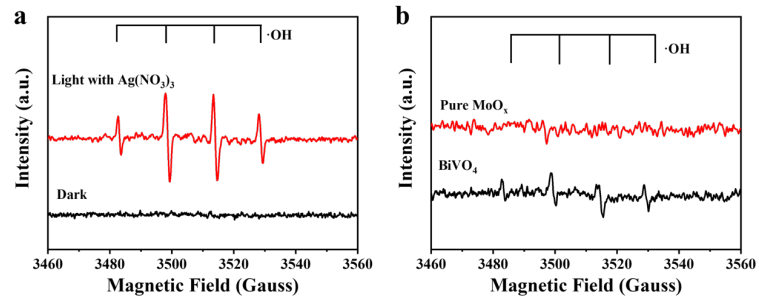


Figure S16. In situ EPR spectra of (a) $BiVO_4$/0.10 $MoO_x$ with 10 mM $Ag(NO_3)_3$ as the electron scavengers. (b) In situ EPR spectra of •H and •OH radicals by using DMPO in an aqueous dispersion of pure $BiVO_4$ and $MoO_x$.

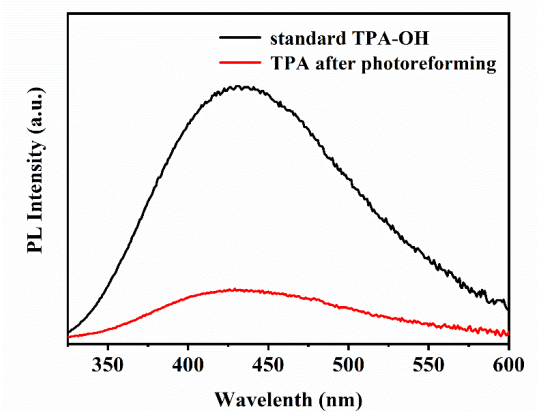


Figure S17. PL spectra of pure TPA-OH and the collected TPA after 5 h of photoreforming.

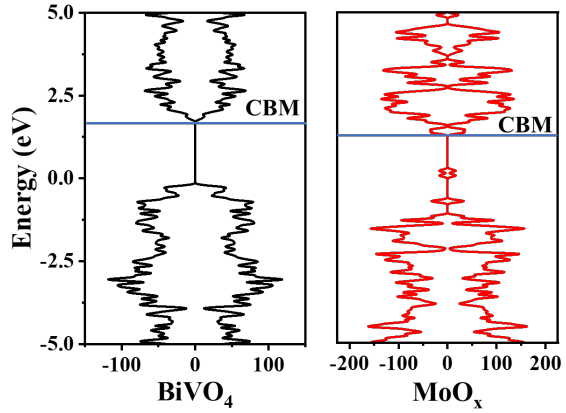


Figure S18. The electronic density of states (DOS) of independent $BiVO_4$ and $MoO_x$ was leveled relative to the deep energy level of $N_2$ gas.

Table S1. Quantification (by 1H-NMR spectroscopy) of polymer (PET and PLA) solubilization after pre-treatment (50 mL, 1M KOH, 48h).

| Sample | Addition | Components | Ideal quantity of component | Measured quantity of component | solubilization |
|---|---|---|---|---|---|
| PET | 1g | ethylene glycol | 0.27 | 0.10 | 37% |
| | | terephthalate | 0.73 | 0.24 | 33% |

Table S2. Plastic photoreforming performance for selected state-of-the-art photocatalysts.

| Plastics | Catalyst | Solvent | Reduction product | Activity/ μmol $g^{-1}h^{-1}$ | Oxidation product | Activity/ μmol $g^{-1}$ $h^{-1}$ | Ref. |
|---|---|---|---|---|---|---|---|
| Pre [a]-PET[b] | $BiVO_4/MoO_x$ | 1M NaOH | $H_2$ | $1.96\times10^3$ | formate | $0.29\times10^3$ | This work |
| | | | | | acetate | $0.19\times10^3$ | |
| Pre-PET | $CdS/CdO_x$ | 10M NaOH | $H_2$ | $3.42\times10^3$ | formate | N/A | [1] |
| PET | Co-$Ga_2O_3$ | Deionized water | $H_2$ | $0.384\times10^3$ | CO | 100.6 | [2] |
| Pre-PET | $CN_x$\|$Ni_2P$ | 1M KOH | $H_2$ | 25.7 | formate | N/A | [3] |
| Pre-PET | $Ag_2O$/Fe-MOF [c] | Deionized water | $H_2$ | $1.9\times10^3$ | N/A | N/A | [4] |
| Pre-PET | MXene/ $Zn_xCd_{1-x}S$ [d] | 10M NaOH | $H_2$ | $14.17\times10^3$ | formate | N/A | [5] |
| Pre-PET | $MoS_2$/CdS | 10 M KOH | $H_2$ | $3.90\times10^3$ | formate | $0.72\times10^3$ | [6] |
| Pre-PET | d-$NiPS_3$/CdS | 2 M KOH | $H_2$ | $31.38\times10^3$ | formate | $2.6\times10^3$ | [7] |
| | | | | | acetate | $1.5\times10^3$ | |
| | | | | | glycolate | $2.8\times10^3$ | |

a) Pre: Pretreated b) PET: polyethylene terephthalate; c) MOF: metal-organic-framework;

Table S3. Product quantification after 5 h photoreforming of pretreated PET (50 mL) by GC, HPLC, and the calculation of charge transfer numbers.

| Products | Amount/mmol | Charge transfer numbers | Total /mmol | Charge balance | Selectivity |
|---|---|---|---|---|---|
| $H_2$ | 0.49 | $e^-$: 0.49*2 | $e^-$: 0.98 | 67% ($h^+$/ $e^-$) | / |
| Formate | 0.0725 | $h^+$: 0.0725*3 | $h^+$: 0.22 | | 20.1% |
| Acetate | 0.0475 | $e^-$: 0.0475*2 | $e^-$: 0.095 | | 26.4% |
| | | $h^+$: 0.0475*4 | $h^+$: 0.19 | | |
| $CO_3^{2-}$ | 0.062 | $h^+$: 0.062*5 | $h^+$: 0.31 | | 17.3% |

**Note: 1)** The $CO_3^{2-}$ obtained by further oxidizing of formate, the reaction pathway as follow:

$HCOO^- + 2h^+ + 3OH^- \rightarrow CO_3^{2-} + 2H_2O$

Moreover, owing to being in the alkaline medium, $CO_3^{2-}$ with an accumulative concentration of 0.062 mmol instead of gaseous $CO_2$ evolution was determined by a self-built methodology.


[1] T. Uekert, M.F. Kuehnel, D.W. Wakerley, E. Reisner, Plastic waste as a feedstock for solar-driven $H_2$ generation, Energ. Environ. Sci., 11 (2018) 2853-2857.

[2] J. Xu, X. Jiao, K. Zheng, W. Shao, S. Zhu, X. Li, J. Zhu, Y. Pan, Y. Sun, Y. Xie, Plastics-to-syngas photocatalysed by Co–Ga2O3 nanosheets, Natl. Sci. Rev., 9 (2022) nwac011.

[3] T. Uekert, H. Kasap, E. Reisner, Photoreforming of Nonrecyclable Plastic Waste over a Carbon Nitride/Nickel Phosphide Catalyst, J. Am. Chem. Soc., 141 (2019) 15201-15210.

[4] J. Qin, Y. Dou, F. Wu, Y. Yao, H.R. Andersen, C. Hélix-Nielsen, S.Y. Lim, W. Zhang, In-situ formation of Ag2O in metal-organic framework for light-driven upcycling of microplastics coupled with hydrogen production, Appl. Catal. B-Environ., 319 (2022) 121940.

[5] B. Cao, S. Wan, Y. Wang, H. Guo, M. Ou, Q. Zhong, Highly-efficient visible-light-driven photocatalytic H2 evolution integrated with microplastic degradation over MXene/ZnxCd1-xS photocatalyst, J. Colloid Interf. Sci., 605 (2022) 311-319.

[6] M. Du, Y. Zhang, S. Kang, X. Guo, Y. Ma, M. Xing, Y. Zhu, Y. Chai, B. Qiu, Trash to Treasure: Photoreforming of Plastic Waste into Commodity Chemicals and Hydrogen over MoS2-Tipped CdS Nanorods, ACS Catal., 12 (2022) 12823-12832.

[7] S. Zhang, H. Li, L. Wang, J. Liu, G. Liang, K. Davey, J. Ran, S.-Z. Qiao, Boosted Photoreforming of Plastic Waste via Defect-Rich NiPS3 Nanosheets, J. Am. Chem. Soc., 145 (2023) 6410-6419.